中国光学（中英文）
Chinese Optics
Ei 核心期刊

High-precision beam pointing control based on global non-singular attitude estimation

GUO Ming, FAN Yi-di, WANG Peng-cheng, AN Ke, LU Wei, CHEN Wen, ZHANG Yong-he, LIN Bao-jun

Citation:
GUO Ming, FAN Yi-di, WANG Peng-cheng, AN Ke, LU Wei, CHEN Wen, ZHANG Yong-he, LIN Bao-jun. High–precision beam pointing control based on global non–singular attitude estimation[J]. *Chinese Optics*, 2026, 19(5): 1–17. doi: 10.3724/CO.EN–2026–0004
郭明, 范一迪, 王鹏程, 安轲, 卢苇, 陈雯, 张永合, 林宝军. 基于全局非奇异姿态估计的星间光束精密指向控制[J]. 中国光学, 2026, 19(5): 1–17. doi: 10.3724/CO.EN–2026–0004

View online: https://doi.org/10.3724/CO.EN–2026–0004

Articles you may be interested in

Optimization of optical metrology noise link metrics for space–based gravitational wave detection spacecraft
空间引力波探测航天器光学测距噪声链路指标优化
Chinese Optics. 2025, 18(3): 568   https://doi.org/10.37188/CO.2024–0185

Calculation of laser interferometric quantum noise in gravitational wave detection
引力波探测中激光干涉量子噪声计算
Chinese Optics. 2025, 18(3): 698   https://doi.org/10.37188/CO.2024–0180

Iterative estimation and precision suppression of inter–spacecraft tilt–to–length coupling noise for the Taiji space gravitational wave detection mission
空间引力波探测“太极计划”星间姿态–光程耦合噪声迭代拟合与高精度抑制方法
Chinese Optics. 2025, 18(3): 583   https://doi.org/10.37188/CO.2025–0042

Research on pointing accuracy of liquid crystal phase array based on the variable period grating method
基于变周期光栅法的液晶相控阵指向精度研究
Chinese Optics. 2025, 18(1): 29   https://doi.org/10.37188/CO.2024–0097

Composite fast nonsingular terminal sliding mode control of fast steering mirror
快速反射镜的复合快速非奇异终端滑模控制
Chinese Optics. 2024, 17(4): 959   https://doi.org/10.37188/CO.2023–0203

Measurement and suppression of forward stray light for spaceborne gravitational wave detection
空间引力波探测前向杂散光测量和抑制
Chinese Optics. 2023, 16(5): 1081   https://doi.org/10.37188/CO.2022–0251

文章编号 2097-1842(2026)05-0001-17

High-precision beam pointing control based on global non-singular attitude estimation

GUO Ming[1,2,3], FAN Yi-di[1,2 *], WANG Peng-cheng[1,2,3], AN Ke[1,2], LU Wei[1,3], CHEN Wen[1,3], ZHANG Yong-he[1,2,3], LIN Bao-jun[1,3]

(1. *Innovation Academy for Microsatellites*, *Chinese Academy of Sciences*, *Shanghai* 201304, *China*;
2. *Key Laboratory for Satellite Digitalization Technology*, *Chinese Academy of Sciences*, *Shanghai* 201210, *China*;
3. *University of Chinese Academy of Sciences*, *Beijing* 100049, *China*)

* *Corresponding author*, *E-mail*: *fanyd@microsate.com*

Abstract: Focusing on the key problem of establishing inter-spacecraft laser links for space-borne gravitational wave (GW) detection, this paper presents a high-precision beam pointing control scheme founded on multi-source information fusion. A detailed state-space model is constructed by integrating the coupled dynamics of moving optical sub-assemblies. Using error quaternions, the nonlinear measurement equations are linearized, thereby enhancing the accuracy of filter-based attitude determination via inertial sensor fusion. Furthermore, a time-varying analytical formulation of the point-ahead angle (PAA) is derived, supplying a theoretical basis for servo compensation. Closed-loop simulations of a three-spacecraft configuration validate the stability and accuracy of the proposed estimation algorithm. In combination with robust disturbance-rejection control, the method enables highly accurate beam pointing, providing essential technical support for GW detection missions.

Key words: gravitational wave detection; beam pointing control; attitude estimation; kalman filter; point-ahead angle

收稿日期:2026-01-08; **修订日期**:xxxx-xx-xx

基金项目:国家重点研发计划(No. 2022YFC2203700, No. 2021YFC2202600);上海市科技创新行动计划(No. 24YF2742600)

This work was supported by National Key R&D Program of China (No. 2022YFC2203700, No. 2021YFC2202600,) and the Shanghai Science and Technology Innovation Action Plan (No. 24YF2742600).

基于全局非奇异姿态估计的星间光束精密指向控制

郭　明[1,2,3], 范一迪[1,2*], 王鹏程[1,2,3], 安　轲[1,2], 卢　苇[1,3], 陈　雯[1,3], 张永合[1,2,3], 林宝军[1,3]
（1. 中国科学院微小卫星创新研究院, 上海 201304;
2. 中国科学院卫星数字化技术重点实验室, 上海 201210;
3. 中国科学院大学, 北京 100049）

摘要: 针对空间引力波探测航天器的星间建链任务, 研究了基于多源信息融合的光束精密指向控制问题。结合引力波探测航天器的结构和载荷特性, 建立包含移动光学组件运动的全系统状态方程, 利用误差四元数将非独立变量描述的非线性测量方程转化为独立变量描述的线性方程, 并融合惯性传感器的测量信息进行滤波估计以提高卫星平台的定姿精度。此外, 针对超远距离星间激光传输时间和两星之间高速相对运动导致的超前指向问题, 推导了随时间变化的超前角解析表达式, 并仿真分析了轨道周期内超前角的变化趋势, 为星间链路建立与维持过程的超前角伺服补偿提供了理论依据。通过三星系统的闭环仿真验证了所设计的高精度指向估计算法在稳定性和估计精度方面的优越性, 结合鲁棒抗扰控制器实现了光束的精密指向, 为我国引力波探测计划的顺利实施提供必要的技术支撑。

关　键　词: 引力波探测; 光路指向控制; 状态估计; 卡尔曼滤波; 超前指向
中图分类号: TP394.1;TH691.9　**文献标志码:** A　**doi:** 10.3724/CO.EN-2026-0004　**CSTR:** 32171.14.CO.EN-2026-0004

1 Introduction

Space-borne gravitational wave observatories use three spacecraft arranged in a triangular formation to create a large, spaceborne laser interferometer. Gravitational-wave signals are identified by tracking changes in the optical path length between each pair of spacecraft[1]. The distance between spacecraft ranges from thousands of kilometers to hundreds of millions of kilometers depending on the measurement band. Currently, the most representative international project is the Laser Interferometer Space Antenna (LISA) [2]. It consists of three spacecraft in a heliocentric orbit, flying in a quasi-equilateral triangular formation with an edge length of 5 million km, aiming to detect GWs in the 0.1 mHz to 1 Hz frequency band. China's GW detection projects mainly include the “Taiji Program” in a heliocentric orbit and the “TianQin Program”in a geocentric orbit. The arm length of “Taiji” Program is 3 million kilometers [3-4], while the “TianQin” Program is about 170,000 kilometers [5-6]. To Achieve and maintain a laser link among three spacecraft over ultra-long distances, high-precision inter-spacecraft beam pointing control is a critical enabling technology [7].

Accurate pointing estimation is a vital prerequisite for achieving precise beam pointing control. The GW detection formation system consists of three spacecraft, each composed of a spacecraft platform (Spacecraft, SC) and two moving optical Subassemblies (MOSAs). Each MOSA includes an optical bench (OB), a telescope (TE), and a test mass (TM). The entire spacecraft has 19 degrees of freedom, involving the 6-DoF pose motion of three rigid bodies (the SC with two TMs) and the single-axis rotation of one MOSA[8]. Each spacecraft’s optical bench includes a high-precision point-ahead angle mechanism that adjusts the outgoing laser axis in response to PAA commands, thereby maintaining stable signal transmission.[9]. Laser pointing is primarily achieved through four degrees of freedom: the spacecraft's attitude and one MOSA's rotation angle. The key factor limiting the pointing estimation accuracy is the precision of the SC's attitude determination [10]. The spacecraft can provide high-precision measurements of beam deviation through differential wavefront sensing (DWS) in its scientific mode [11], However, during the laser link acquisition and tracking phase, it is essential to develop robust spacecraft attitude determination methods by integrating ground navigation data with on-board available sensor measurements.

Spacecraft attitude determination methods are mainly divided into two categories: deterministic methods and state estimation methods. The accuracy of deterministic methods is heavily sensitive to measurement precision and it is difficult to establish an attitude model that includes system motion information or handle uncertain parameters in the measurement model. Therefore, high-precision attitude determination typically employs state estimation methods. State estimation methods combine sensor measurement information with a system's dynamic model. Under a given estimation criterion, they can effectively suppress the influence of measurement uncertainty to obtain an optimal or suboptimal solution for the estimated state. The Kalman filter is a mature method widely used in various fields such as spacecraft control, industrial control , radar signal processing, and so on. Spacecraft attitude is usually described by quaternions, which effectively avoid rotational singularities and complex trigonometric calculations. However, its measurement model exhibits strong nonlinearity, making attitude estimation essentially a nonlinear filtering problem. Applying nonlinear filtering algorithms directly to a 19-DoF strongly coupled multi-body system can lead to issues like large computational load, slow convergence, and divergence. Moreover, since the four parameters of a quaternion are not independent variables, directly using a Kalman filter may cause the error covariance matrix to become singular. ZHANG Donglin et al. [12] linearized the nonlinear measurement equation by using the linear mapping relationship between the error quaternion and Euler angles under the small-angle assumption to perform filtering of the spacecraft's attitude. However, this linear mapping is only valid near zero Euler angles and cannot be applied to the global motion estimation of the spacecraft's attitude. The Multiplicative Extended Kalman Filter (MEKF) [13] achieves global non-singular attitude estimation by estimating an unconstrained three-component attitude error parameter and updating the attitude using quaternion multiplication. For the GW detection spacecraft studied in this paper, achieving precise beam pointing estimation requires considering the coupling effect of MOSA motion on the SC's attitude and measurement information from the Gravitational Reference Sensor (GRS) to solve the global attitude estimation problem.

Furthermore, taking the "Taiji Program" spacecraft formation as an example, for an inter-spacecraft distance of about 3 million kilometers, the light travel-time from the transmitting optical bench to the remote receiving one is approximately 10 seconds. Due to the relative motion between adjacent spacecraft and the extremely small laser divergence angle (about 2 μrad), to achieve precise beam pointing, the direction of the transmitted laser must be adjusted by a PAA relative to the incident laser to ensure the alignment accuracy of the optical axes [14-15].

This paper focuses on the inter-spacecraft laser link acquisition task for space-borne GW detection spacecraft, using the "Taiji Program" as an example. It investigates the problem of high-precision beam pointing control based on multi-source information fusion, provides an analytical expression for the transmitted laser's PAA, and proposes a Kalman filtering algorithm with globally linearized quaternion measurement to achieve real-time, high-precision estimation of the spacecraft's attitude. Integrating a robust disturbance rejection controller, this work achieves precise beam pointing, acquisition, and laser link establishment. A comprehensive state-space model is developed by incorporating spacecraft structural characteristics and MOSA dynamics. To enhance attitude determination accuracy, an error-quaternion approach is employed to linearize the constrained, nonlinear measurement equations, enabling the optimal fusion of inertial sensor data. Furthermore, a time-varying analytical expression for the PAA is derived to compensate for propagation delays and inter-spacecraft motion. The evolution of the PAA over an orbital period is analyzed through simulation, providing a theoretical basis for its compensation during laser link maintenance. Constellation-wide closed-loop simulations validate the stability and accuracy of the proposed algorithm, offering critical technical support for space-borne GW detection missions.

2 System Description

2.1 System Motion Model

The laser link system of the three gravitation wave detection spacecrafts is shown in Fig. 1. The dynamics of the three spacecraft are mutually independent. The structure of each spacecraft is shown in Fig. 2, where MOSA1 is fixed to the SC, and MOSA2 can rotate in the spacecraft plane to change breathing angle (±1°), and it not only changes the center of mass and moment of inertia of the entire system but also affects the pose of the SC and the test masses relative to the inertial frame through dynamic coupling. Therefore, this paper first establishes the motion model of the entire system, including the SC (excluding MOSAs and test masses), the 2 MOSAs, and the 2 test masses. Based on the rigid body assumption, the kinematics and dynamics of each part are described. During the modeling process, changes in the mass distribution of the SC due to factors like fuel consumption are ignored. Also, since the pose motion of the two test masses is constrained within a very small space inside their respective electrode housings, it is reasonable to assume their attitude angular displacements are small quantities.

The coordinate systems involved in the modeling process are:

Inertial Frame $\sum_i$**:** The J2000 heliocentric inertial coordinate system defined according to the conventions of the International Celestial Reference System.

SC Frame $\sum_b(x_b y_b z_b)$**:** Fixed to the SC, with the origin located at the SC's center of mass. The x-axis points along the angle bisector of the two MOSA optical axes, the z-axis coincides with the normal of the plane defined by the two MOSA optical axes, and the y-axis is determined by the right-hand rule.

MOSA Frame $\sum_{Ti}(x_{Ti}y_{Ti}z_{Ti})(i=1,2)$**:** Fixed to the corresponding MOSA, with the origin located at the MOSA's center of mass. The x-axis is aligned with the MOSA optical axis pointing at the laser emission direction, the z-axis is parallel to the z-axis of the spacecraft frame, and the y-axis is determined by the right-hand rule.

TM Frame $\sum_{tmi}(x_{tmi}y_{tmi}z_{tmi})$: Fixed to the corresponding TM, with the origin located at the TM's center of mass. Under nominal conditions, the TM frame coincides with the corresponding MOSA frame.

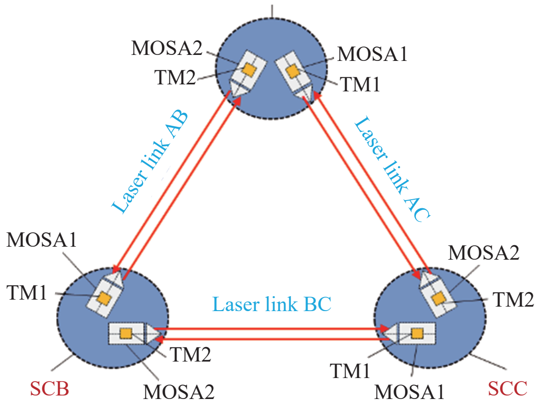

Fig. 1 Formation of the GW detection spacecrafts

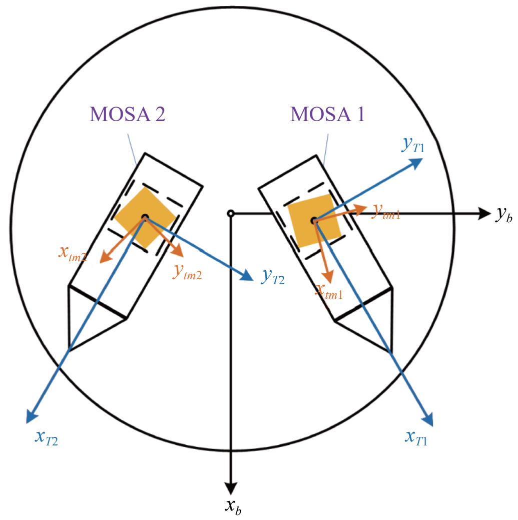

Fig. 2 Structure of each spacecraft with MOSAs and TMs

To simplify the formula derivation, the pose states of the TMs are denoted as $\boldsymbol{x}_{tm} = \left[\boldsymbol{r}_{\mathrm{T1}tm1}^{T}, \boldsymbol{\Phi}_{\mathrm{T1}tm1}^{T}, \boldsymbol{r}_{\mathrm{T2}tm2}^{T}, \boldsymbol{\Phi}_{\mathrm{T2}tm2}^{T}\right]^{\mathrm{T}}$ and, $\boldsymbol{v}_{tm} = \left[\boldsymbol{v}_{\mathrm{T1}tm1}^{T}, \boldsymbol{\omega}_{\mathrm{T1}tm1}^{T}, \boldsymbol{v}_{\mathrm{T2}tm2}^{T}, \boldsymbol{\omega}_{\mathrm{T2}tm2}^{T}\right]^{\mathrm{T}}$ where $\boldsymbol{r}_{T1tm1}$, $\boldsymbol{v}_{T1tm1}$, $\boldsymbol{r}_{T2tm2}$, $\boldsymbol{v}_{T2tm2}$ represent the position and velocity vectors of the centers of mass of TM1 and TM2 relative to the centers of their respective electrode housings, and $\boldsymbol{\Phi}_{T1tm1}$, $\boldsymbol{\omega}_{T1tm1}$, $\boldsymbol{\Phi}_{T2tm2}$, $\boldsymbol{\omega}_{T2tm2}$ represent the attitude angles and angular velocity vectors of TM1 and TM2 relative to their respective electrode housings.

The system state vector is defined as $\boldsymbol{x} = [\boldsymbol{x}_1^{\mathrm{T}}, \boldsymbol{x}_2^{\mathrm{T}}]^{\mathrm{T}}$, $\boldsymbol{x}_1^{\mathrm{T}} = \left[\boldsymbol{x}_{tm}^{T}, \boldsymbol{r}_b^{\mathrm{T}}, \boldsymbol{Q}_b^{\mathrm{T}}, \alpha_{b\mathrm{T2}}\right]_{1\times 20}$, $\boldsymbol{x}_2^{\mathrm{T}} = \left[\boldsymbol{v}_{tm}^{T}, \boldsymbol{v}_b^{\mathrm{T}}, \boldsymbol{\omega}_b^{\mathrm{T}}, \omega_{b\mathrm{T2}}\right]_{1\times 19}$, where $\boldsymbol{r}_b$ and $\boldsymbol{v}_b$ represent the position and velocity vectors of the SC center of mass relative to the inertial frame, $\boldsymbol{Q}_b = [q_0, \boldsymbol{q}_v^{\mathrm{T}}]^{\mathrm{T}}$ and $\boldsymbol{\omega}_b$ represent the attitude quaternion and angular velocity of the SC relative to the inertial frame, α_{bT2} and ω_{bT2} represent the rotation angle and angular velocity of MOSA2 about the z-axis of the SC frame. As the SC attitude is represented by a quaternion, the resulting state vector is 20-dimensional. The system kinematic equations:

$$\dot{x}_1 = K x_2 \quad , \tag{1}$$

where the coefficient matrix is denoted as ***K:***

$$\boldsymbol{K} = \begin{bmatrix} \boldsymbol{E}_{12} & & & \\ & \boldsymbol{E}_3 & & \\ & & \frac{1}{2}\begin{bmatrix} -\boldsymbol{q}_v^{\mathrm{T}} \\ q_0 \boldsymbol{E}_3 + \boldsymbol{q}_v^{\times} \end{bmatrix} & \\ & & & 1 \end{bmatrix}_{20\times 19}$$

By applying the Newton-Euler method, the system dynamic equations can be derived as:

$$\boldsymbol{M}\dot{\mathbf{x}}_2 = \boldsymbol{M}\boldsymbol{\Omega}\boldsymbol{x}_1 + \boldsymbol{B}\boldsymbol{u} + \boldsymbol{G}\boldsymbol{d} \quad , \tag{2}$$

M denotes the system inertia matrix, Ω denotes the coupling stiffness matrix between the acceleration and displacement of the TMs, and B is the input coefficient matrix. The control input is $\boldsymbol{u} = \left[\boldsymbol{f}_{1a}^{\mathrm{T}}, \boldsymbol{l}_{1a}^{\mathrm{T}}, \boldsymbol{f}_{2a}^{\mathrm{T}}, \boldsymbol{l}_{2a}^{\mathrm{T}}, \boldsymbol{f}_{\mathrm{FEEP}}^{\mathrm{T}}, \boldsymbol{l}_{\mathrm{FEEP}}^{\mathrm{T}}, l_{mosa2}\right]^{\mathrm{T}}$, where $\boldsymbol{f}_i$ represent the output force of the inertial sensors and the micro-thrusters, $\boldsymbol{l}_i (i = 1a, 2a, \mathrm{FEEP})$ represent the torque of the inertial sensors and the micro-thrusters, and l_{mosa2} is the driving torque controlling MOSA2. The $\boldsymbol{d}$ denotes the total disturbance, including nonlinear dynamics, dynamic uncertainties, environmental perturbations and actuation noise. $\boldsymbol{G}$ is the disturbance coefficient matrix, and $\boldsymbol{E}_i$ represents the i-dimensional identity matrix.

Therefore, the equations of motion for the entire spacecraft system can be expressed as:

$$\begin{bmatrix} \dot{\mathbf{x}}_1 \\ \dot{\mathbf{x}}_2 \end{bmatrix} = \begin{bmatrix} \mathbf{0} & \boldsymbol{K} \\ \Omega & \mathbf{0} \end{bmatrix} \begin{bmatrix} \boldsymbol{x}_1 \\ \boldsymbol{x}_2 \end{bmatrix} + \begin{bmatrix} \mathbf{0} \\ \boldsymbol{M}^{-1}\boldsymbol{B} \end{bmatrix} \boldsymbol{u} + \begin{bmatrix} \mathbf{0} \\ \boldsymbol{M}^{-1}\boldsymbol{G}\boldsymbol{d} \end{bmatrix}, \tag{3}$$

Note: During inter-spacecraft laser link acquisition, each spacecraft must independently establish two laser links to each of the two remote peers. For example, when spacecraft B is establishing the laser link with spacecraft C, the A–B optical link must be remained intact. Furthermore, the pointing, acquisition and tracking of the laser signal during laser link acquisition should be performed using only the SC attitude maneuver and rotation of MOSA2. Therefore, achieving high-precision, 4-DoF pointing requires coordinated control of the spacecraft attitude and MOSA2 rotation.

2.2 Measure System Model

The star tracker generally outputs the spacecraft body attitude in the form of a quaternion, and the measurement can be expressed as:

$$\boldsymbol{Q}_b^m = \boldsymbol{Q}_b \otimes \boldsymbol{Q}_n \quad , \tag{4}$$

where $\boldsymbol{Q}_b$ denotes the true spacecraft attitude quaternion relative to the inertial frame, and $\boldsymbol{Q}_n$ represents the measurement noise, satisfying:

$$\boldsymbol{Q}_n \approx \begin{bmatrix} 1 \\ \boldsymbol{\eta}_{str} \end{bmatrix} \quad , \tag{5}$$

The measurement noise of the star tracker typically consists of white noise and slowly varying errors. The latter may arise from thermal imbalance within one orbital period or from aberration effects due to relative motion between the observer and the light source. However, for the heliocentric orbit of the GW detector studied in this paper, the influence of slowly varying errors can be neglected, and the measurement noise $\boldsymbol{\eta}_{str}$ is treated as white noise.

According to the readout noise model of the GRS shown in Fig. 3[16], the readout noise can be approximated as white noise in the frequency range above 1 mHz Therefore, the measurement outputs of the two test masses can be expressed as:

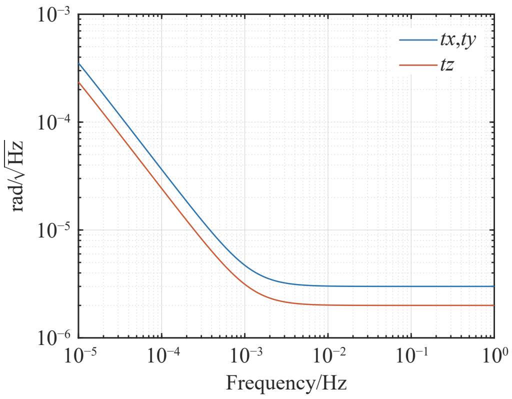

(a) TM position measurement noise

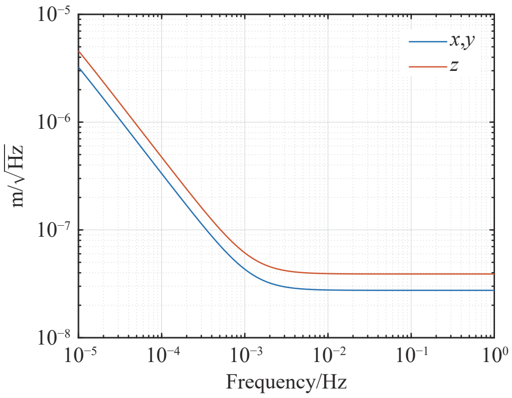

(b) TM rotation measurement noise

Fig. 3 TM measurement noise model

$$\boldsymbol{x}_{tm}^{m} = \boldsymbol{x}_{tm} + \boldsymbol{\eta}_{grs} \quad , \tag{6}$$

where $\boldsymbol{x}_{tm}$ denotes the true pose of the two test masses, and $\boldsymbol{\eta}_{grs}$ represents the measurement noise.

The rotational motion of MOSA2 about the pivot axis perpendicular to the spacecraft plane is driven by a piezoelectric actuator. Its measured rotation angle α_{bT2}^{m} is related to the true rotation angle α_{bT2} and the measurement noise η_{mosa} by:

$$\alpha_{bT2}^{m} = \alpha_{bT2} + \eta_{mosa} \quad , \tag{7}$$

3 Precise pointing control strategy

The constellation acquisition phase is inherently challenging due to the vast distances between spacecrafts. Before the laser link is established, the SC and MOSA point control method is based on ground navigation data. However, due to navigation errors, sensor measurement errors, and installation misalignments, the transmitting spacecraft's laser cannot precisely hit the counterpart. Even though the receiving spacecraft's Charge-Coupled Device (CCD) has a relatively large detection field of view (FoV), it may still fail to capture the incoming laser. Therefore, the transmitting spacecraft must perform a coverage scan over the uncertain celestial region of the receiver according to a scanning guidance law. Only when the CCD detects the laser signal can the spacecraft correct its pointing based on the measurement, ensuring that its laser enters the receiver's CCD FoV. Subsequently, both spacecraft can refine their laser pointing so that the signal falls within the counterpart's Quadrant Photodiode (QPD) FoV, enabling more precise pointing and frequency corrections until the laser interferometric measurement is established.

3.1 Laser link acquisition strategy

The single-link acquisition procedure generally comprises four stages:

1) **Pre-pointing**: Based on the ground navigation data, the spacecraft would adjust their attitudes and the rotation angle of MOSA2, so that the two MOSA optical axes are roughly aligned with the remote spacecraft.

2) **Scan and acquisition:** The transmitting spacecraft scans along a pre-defined spiral line that covers the uncertainty cone where the receiving spacecraft is located. After the receiving spacecraft's CCD capturing the laser signal, the receiver adjusts its attitude to align its optical axis with the incoming direction and then turns on its beam. When the transmitter finishes its scan and turns off its laser, it then uses the CCD detection to refine their pointing to make sure that its MOSA optical axis is aligned with the incoming direction. At this point, both ends have acquired each other's signals.

3) **Rough correction:** If the QPD does not de-

tect the signal, the two spacecrafts switch their laser beam on and off in turn and then use CCD to reduce pointing offsets until the incoming laser enters the QPD field. If the beam is already in the QPD field after scanning, this step can be omitted.

4) **Fine correction**: Using the data of differential wavefront sensing from the QPD, both spacecrafts further adjust pointing directions of the MOSA optical axis and perform laser frequency scanning to establish the inter-spacecraft interferometric measurement.

After the above procedure is completed for one arm, the other two arms are acquired to orderly use the same method to form the complete three-arm interferometer, which meet the requirements of scientific detection.

3.2 Point-Ahead Angle Calculation

For a GW detection formation with an inter-spacecraft distance of approximately 3 million kilometers, when spacecraft A emits a laser beam towards spacecraft B, the beam flies about 10 seconds to reach the spacecraft B. At this moment, spacecraft B can detect the laser signal from A only if it lies within the divergence angle of the beam and its receiving optical bench is aligned with the incoming laser direction. Meanwhile, the transmitting OB of spacecraft B must point its laser towards the position that spacecraft A will reach about 10 seconds later, so that the beam to be detected by spacecraft A's receiving optical bench (assuming that A's receiver is aligned with the incoming direction). Therefore, in inter-spacecraft laser links for spaceborne GW detection, the control of point-ahead pointing must be incorporated to ensure both beams pointing accuracy and tracking accuracy during acquisition and tracking processes.

The angle formed between the negative direction vector of the incident laser (pointing towards the transmitting spacecraft) and the transmitting laser direction vector (pointing toward the receiving spacecraft) at the same optical bench of spacecraft B is defined as the PAA. As illustrated in Fig. 4, the red dashed lines represent the vector of the laser that is received by spacecraft B MOSA1 and emitted from B MOSA1 to spacecraft A. The angle α denotes the PAA corresponding to MOSA1 of spacecraft B.

Since the triangular three-spacecraft formation undergoes both heliocentric orbital motion and rotation about the formation center within the plane, the PAAs of each spacecraft vary periodically with the orbital motion. Each optical bench is therefore equipped with a two-dimensional PAAM to correct the varying PAA. The following derivation takes the optical link associated with MOSA1 of spacecraft B as an example to establish the calculation formula for the PAA.

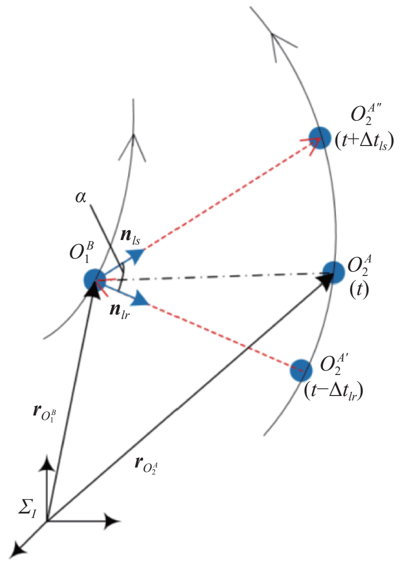

Fig. 4　Point-ahead angle representation

First, because the formation centroid orbit coincides with Earth's orbit, the actual orbits of the spacecraft can be approximated as circular. Within the timescale relevant to calculating the laser direction vectors and the PAA, it is reasonable to assume that the spacecrafts undergo uniform circular motion. Thus, the propagation time of the beam Δt_l between two spacecraft satisfies the relation:

$$\|\boldsymbol{R}_{AB} + \boldsymbol{V}_{AB} \cdot \Delta t_l\| = \Delta t_l \cdot c \quad , \qquad (8)$$

where c denotes the speed of light, and $\boldsymbol{R}_{BA}$ and $\boldsymbol{V}_{BA}$ represent the relative position and velocity vectors of spacecraft A relative to spacecraft B.

Considering the finite propagation time of the laser beam between spacecraft, the directions of the received and transmitted beams at two spacecraft are no longer coincident, as illustrated in Fig. 4. Assuming that each spacecraft optical bench can be approximated as a mass point, at time t the optical bench of MOSA1 on spacecraft B $BO1$ is located at pointO_1^B, and the optical bench of MOSA2 on spacecraft A $AO2$is located at pointO_2^A. At this moment, the direction vector of the incident laser received by $BO1$ is$-\boldsymbol{n}_{lr}$. The actual incident beam, shown as the red dashed line, was emitted from $AO2$at time$(t-\Delta t_{lr})$and detected by B at time t. Let the position of spacecraft A at time$(t-\Delta t_{lr})$be denoted as$O_2^{A}{}'$,thus the beam propagates from $O_2^{A}{}'$toO_1^B over the propagation timeΔt_{lr}. Similarly, at time t, $BO1$emits a laser along the direction vector $\boldsymbol{n}_{ls}$ (red dashed line). After a propagation time of Δt_{ls}, the beam is detected by spacecraft A at time $(t+\Delta t_{ls})$, when A has moved to point $O_2^{A}{}''$. According to the definition of the PAA, the PAA of spacecraft B's MOSA1 at time t is given by:

$$PAA_{BO1} = \arcsin(\|\boldsymbol{n}_{lr} \times \boldsymbol{n}_{ls}\|) \quad , \qquad (9)$$

Considering that the PAA adjusts the transmitted laser direction based on the MOSA optical axis, while the control of the spacecraft attitude and the MOSA2 rotation angle aims to align both MOSA optical axes with the incoming laser direction, we define a plane $\boldsymbol{S}$ spanned by the incident laser beams of the two MOSA optical benches. The PAA is then decomposed into an in-plane angle$PAA_{BO1,ip}$and an out-of-plane angle $PAA_{BO1,op}$relative to plane $\boldsymbol{S}$. The projection of the transmitted laser direction vector onto plane $\boldsymbol{S}$ be denoted as $\boldsymbol{n}_{ls,pro}$, then:

$$PAA_{BO1,ip} = \arcsin\left(\left\|\boldsymbol{n}_{lr} \times \frac{\boldsymbol{n}_{ls,pro}}{\|\boldsymbol{n}_{ls,pro}\|}\right\|\right) \quad , \qquad (10)$$

$$PAA_{BO1,op} = \arcsin\left(\left\|\boldsymbol{n}_{ls} \times \frac{\boldsymbol{n}_{ls,pro}}{\|\boldsymbol{n}_{ls,pro}\|}\right\|\right) \quad , \qquad (11)$$

To evaluate the influence of the PAA on precise inter-spacecraft laser pointing, a simulation was carried out considering only the gravitational perturbations of the Sun and the eight planets. The variation of the PAAs corresponding to the optical benches on both sides of the three-spacecraft system was simulated over one year, with the results shown in Fig. 5. It can be observed that the out-of-plane PAA vary periodically around zero with peak-to-peak values of 3.98×10^{-4}rad6.90×10^{-6}rad, and the in-plane PAA vary periodically around -1.985×10^{-6}rad, with peak-to-peak values 4.0×10^{-8}rad.

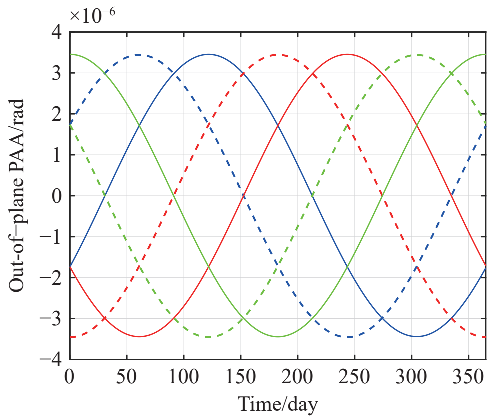

(a) Out-of-plane PAA

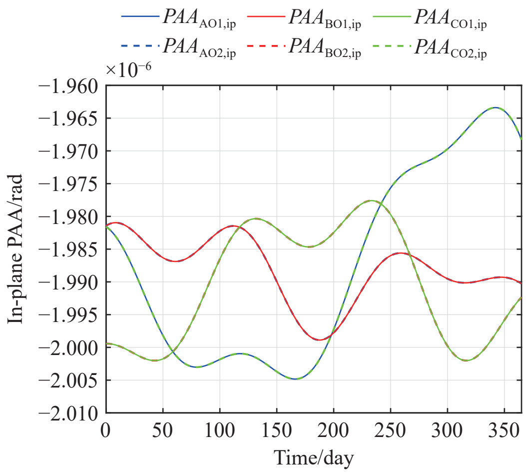

(b) In-plane PAA

Fig. 5 PAA change of the 3 spacecrafts during an orbit period

Moreover, for the same optical link, the two in-plane PAAs at opposite ends of the laser link exhibit equal magnitudes with opposite signs. Considering that the divergence half-angle of the laser beam is approximately 2 μrad, in precision beam pointing control, variations of the transmitted laser PAA must be compensated by adjusting the transmission direction through the PAAM.

3.3 Pointing Error Calculation

In the process of establishing an inter-spacecraft laser link, a spacecraft's laser pointing measurement primarily relies on the star tracker, CCD, and QPD. Since the measurement outputs of the MOSAs and their expected commands differ in form, pointing errors can be classified into two types:

1. Before the CCD detects the laser: Only the star tracker provides valid output. At this stage, the expected pointing is represented by the direction vector derived from ground navigation or the guidance law.

2. After the CCD or QPD detects the laser: In addition to the star tracker, the measurement output includes the 2D angular deviation of the incident laser in the CCD or QPD measurement plane. The expected pointing is then defined as the direction that positions the incident laser at the center of the measurement plane.

For these two cases, the SC attitude error and MOSA2 angular error are provided as inputs to the pointing controller.

1. Desired Direction Vector

Taking spacecraft B as an example, let the desired pointing directions of the MOSA optical axis be denoted as $\boldsymbol{V}_{S1}$ and $\boldsymbol{V}_{S2}$. The current attitude of the SC with respect to the inertial frame is $\boldsymbol{R}_{ib}$, and the rotation angle of MOSA2 relative to its nominal position is α_{bT2}. According to the definition of $\sum_{T1}$, its transformation matrix between the corresponding frames $\sum_b$ can be written as $\boldsymbol{R}_{bT1}$. Based on the desired optical axis vectors $\boldsymbol{V}_{S1}$ and $\boldsymbol{V}_{S2}$, an intermediate coordinate frame can be denoted as $\sum_{c1}$, whose basis vectors are given by:

$$\begin{aligned} \boldsymbol{e}_{c1x} &= \frac{\boldsymbol{V}_{S1}}{\|\boldsymbol{V}_{S1}\|} \\ \boldsymbol{e}_{c1z} &= \frac{\boldsymbol{V}_{S2}\times\boldsymbol{V}_{S1}}{\|\boldsymbol{V}_{S2}\times\boldsymbol{V}_{S1}\|} \\ \boldsymbol{e}_{c1y} &= \boldsymbol{e}_{c1z}\times\boldsymbol{e}_{c1x} \end{aligned} \quad , \tag{12}$$

Therefore, based on the overall spacecraft geometric configuration, the current SC attitude error and the MOSA2 rotation angle error can be calculated as follows:

$$\Delta\boldsymbol{R}_b = \left(\boldsymbol{R}_{bT1}^{-1}\cdot\boldsymbol{R}_{ic1}\right)\cdot\boldsymbol{R}_{ib}^{-1} \quad , \tag{13}$$

$$\Delta\alpha_{bT2} = \alpha_{bT2} - \left(\frac{\pi}{3} - \arcsin\left(\|\boldsymbol{V}_{S2}\times\boldsymbol{V}_{S1}\|\right)\right) \quad , \tag{14}$$

2. Two-Dimensional Angular Deviation Measurement

Let the angle-of-arrival measurements of the incident lasers on both sides of the local spacecraft be denoted as $[\lambda_1,\eta_1],[\lambda_2,\eta_2]$ (where both $\lambda_1,\eta_1,\lambda_2,\eta_2$ are small quantities). Then, the negative direction vectors of the incident lasers (pointing from the local SC to the remote SC), expressed in the corresponding MOSA frames, can be written as:

$$\boldsymbol{L}_{1m}^{c1} = \begin{bmatrix} 1 \\ -\lambda_1 \\ \eta_1 \end{bmatrix}, \boldsymbol{L}_{2m}^{c2} = \begin{bmatrix} 1 \\ -\lambda_2 \\ \eta_2 \end{bmatrix} \quad , \tag{15}$$

Ideally, after attitude correction, we have $\boldsymbol{L}_{1m}^{c1}=[1,0,0]^{\mathrm{T}}$ and $\boldsymbol{L}_{2m}^{c2}=[1,0,0]^{\mathrm{T}}$.

$$\begin{bmatrix} 1 \\ 0 \\ 0 \end{bmatrix} = \boldsymbol{R}_{bT1}\cdot\Delta\boldsymbol{R}_b\cdot\boldsymbol{R}_{bT1}^{-1}\cdot\boldsymbol{L}_{1m}^{c1} \quad , \tag{16}$$

$$\begin{bmatrix} 1 \\ 0 \\ 0 \end{bmatrix} = \Delta\boldsymbol{R}_\alpha\cdot\boldsymbol{R}_{bT2}\cdot\Delta\boldsymbol{R}_b\cdot\boldsymbol{R}_{bT2}^{-1}\cdot\boldsymbol{L}_{2m}^{c2} \quad , \tag{17}$$

$\Delta\boldsymbol{R}_b$ denotes the current SC attitude error, $\Delta\boldsymbol{R}_\alpha$ denotes the rotation transformation matrix corresponding to the rotation angle $\Delta\alpha_{bT2}$ about the z-axis, and $\boldsymbol{R}_{bT2}$ denotes the transformation matrix of frame $\sum_{T2}$ relative to the reference frame. Based on the assumption that pointing errors are small quantities, the corresponding SC attitude errors (denoted by the Euler angles θ,φ,ψ for the x, y, and z-axes) and the MOSA2 rotation angle error can be obtained as:

$$\begin{bmatrix} \theta \\ \varphi \\ \psi \\ \Delta\alpha_{bT2} \end{bmatrix} = \begin{bmatrix} 0 & 1 & 0 & -1 \\ 0 & \frac{-1}{\sqrt{3}} & 0 & -\frac{1}{\sqrt{3}} \\ -1 & 0 & 0 & 0 \\ 1 & 0 & -1 & 0 \end{bmatrix} \begin{bmatrix} \lambda_1 \\ \eta_1 \\ \lambda_2 \\ \eta_2 \end{bmatrix}, \tag{18}$$

At this stage, during the attitude correction process of the SC, the measurement output of the star tracker is not used. Instead, the two-dimensional beam angular deviation measurement with higher accuracy is directly applied to determine the current SC attitude, thereby avoiding interference of star tracker measurement noise with precise pointing.

Note: When only one side of MOSA receives a detection signal, the two-dimensional AoA measurement cannot directly determine the full three-dimensional SC attitude. In this case, the star tracker measurements must be employed. The two-dimensional AoA measurements can be converted into a spatial vector and then substituted into the first case to compute the pointing error.

3.4 Pointing Control Based on MEKF

For the three-spacecraft formation system in GW detection, each SC must not only maintain a specific attitude such that the optical axes of its two MOSAs point to the remote spacecraft to form the inter-spacecraft laser links but also preserve the triangular laser link structure rotating around the formation barycenter within the formation plane. Consequently, the three-axis attitude motion of the SC involves the space$[0, 2\pi)$. To avoid singularities and complicated trigonometric operations, the spacecraft attitude is represented using quaternions. However, the attitude equations expressed in quaternion form are nonlinear. Direct application of nonlinear filtering methods to the full 19-degree-of-freedom spacecraft system leads to excessive computational load, slow convergence, and possible divergence. Furthermore, attitude quaternions are not independent parameters and must satisfy the normalization constraint, which may introduce degeneracy in the derivation process. Therefore, in this paper, the error quaternion is employed to reduce the attitude equations into three independent components, and then, in combination with inertial sensor measurements, the extended Kalman filter (EKF) is applied to provide a global non-singular attitude estimation for the SC.

3.4.1 State equations

For the GW detection spacecraft formation system, during the process of inter-spacecraft laser link establishment, the position and velocity vectors of the SC's center of mass in the inertial frame are unobservable. Therefore, based on the system motion equation (3) and by selecting the state variables $\boldsymbol{X} = [\boldsymbol{X}_1^{\mathrm{T}}, \boldsymbol{X}_2^{\mathrm{T}}]^{\mathrm{T}}_{1\times32}, \boldsymbol{X}_1 = [\boldsymbol{x}_{tm}^{\mathrm{T}}, \boldsymbol{q}_v^{\mathrm{T}}, \alpha_{b\mathrm{T}2}]^T_{1\times16}, \boldsymbol{X}_2 = \left[\boldsymbol{\upsilon}_{tm}^{\mathrm{T}}, \boldsymbol{\omega}_b^{\mathrm{T}}, \omega_{b\mathrm{T}2}\right]^T_{1\times16}$, the state-space form describing the TM pose, SC attitude, and MOSA2 rotation angle ,along with their respective angular velocities can be obtained:

$$\begin{cases} \dot{\boldsymbol{x}}_{tm} = \boldsymbol{\upsilon}_{tm} \\ \dot{\boldsymbol{Q}}_b = \frac{1}{2}(q_0 - \boldsymbol{q}_v^{\mathrm{T}} + \boldsymbol{q}_v^{\times})\boldsymbol{\omega}_b \\ \dot{\alpha}_{bT2} = \omega_{bT2} \end{cases}, \qquad (19)$$
$$\dot{\boldsymbol{X}}_2 = \Omega \boldsymbol{X}_1 + \boldsymbol{M}^{-1}\boldsymbol{B}\boldsymbol{u} + \boldsymbol{M}^{-1}\boldsymbol{G}\boldsymbol{d}$$

Here, $\boldsymbol{X}_1 = [\boldsymbol{x}_{tm}^{\mathrm{T}}, \boldsymbol{q}_v^{\mathrm{T}}, \alpha_{b\mathrm{T}2}]^T_{1\times16}$, $\boldsymbol{X}_2 = \left[\boldsymbol{\upsilon}_{tm}^{\mathrm{T}}, \boldsymbol{\omega}_b^{\mathrm{T}}, \omega_{b\mathrm{T}2}\right]^T_{1\times16}$,$\boldsymbol{M}$, $\boldsymbol{B}$ and $\boldsymbol{G}$ denote the reorganized coefficient matrices obtained from equation (2) after removing the rows and columns corresponding to $\boldsymbol{r}_b$ and $\boldsymbol{\upsilon}_b$. The estimated values of each state variable are as follows:

$$\begin{cases} \dot{\hat{\boldsymbol{x}}}_{tm} = \hat{\boldsymbol{\upsilon}}_{tm} \\ \dot{\hat{\boldsymbol{Q}}}_b = \frac{1}{2}(\hat{q}_0 - \hat{\boldsymbol{q}}_v^{\mathrm{T}} + \hat{\boldsymbol{q}}_v^{\times})\hat{\boldsymbol{\omega}}_b \\ \dot{\hat{\alpha}}_{bT2} = \hat{\omega}_{bT2} \end{cases},$$
$$\dot{\hat{\boldsymbol{X}}}_2 = \Omega \hat{\boldsymbol{X}}_1 + \boldsymbol{M}^{-1}\boldsymbol{B}\boldsymbol{u} \qquad (20)$$

From the equation(19), it can be seen that except for the kinematic equations of the SC attitude, all others are linear. Therefore, the estimation errors of the test mass pose and MOSA2 rotation angle are given by:

$$\begin{aligned} \Delta \boldsymbol{x}_{tm} &= \boldsymbol{x}_{tm} - \hat{\mathbf{x}}_{tm} \\ \Delta \alpha_{bT2} &= \alpha_{bT2} - \hat{\alpha}_{bT2} \end{aligned}, \qquad (21)$$

The deviation between the true value$\boldsymbol{X}_2$and its estimated value$\hat{\mathbf{X}}_2$ is:

$$\Delta \boldsymbol{X}_2 = \boldsymbol{X}_2 - \hat{\mathbf{X}}_2 \quad , \qquad (22)$$

By differentiating both sides of the equation (21) and (22), the state deviation equations corresponding to each degree of freedom can be obtained:

$$\begin{aligned}\Delta\dot{\mathbf{x}}_{tm} &= \Delta\hat{\boldsymbol{\upsilon}}_{tm}\\ \Delta\dot{\alpha}_{bT2} &= \Delta\hat{\omega}_{bT2}\\ \Delta\dot{\mathbf{X}}_2 &= \Omega\Delta\hat{\mathbf{X}}_1\end{aligned} \quad , \qquad (23)$$

For the nonlinear SC attitude kinematic equations represented by quaternions, let $\Delta\boldsymbol{Q}_b = [\Delta q_0, \Delta\boldsymbol{q}_v^{\mathrm{T}}]^{\mathrm{T}}$ denote the error quaternion between the true attitude quaternion $\boldsymbol{Q}_b$ and the estimated quaternion $\hat{\mathbf{Q}}_b$. Then the following relation holds among the three:

$$\boldsymbol{Q}_b = \hat{\mathbf{Q}}_b \otimes \Delta\boldsymbol{Q}_b \quad , \qquad (24)$$

By differentiating both sides of the equation and substituting the SC attitude kinematic equations, we obtain:

$$\Delta\dot{\boldsymbol{Q}}_b = \frac{1}{2}\Delta\boldsymbol{Q}_b \otimes \begin{bmatrix} 0 \\ \hat{\boldsymbol{\omega}}_b \end{bmatrix} + \frac{1}{2}\Delta\boldsymbol{Q}_b \otimes \begin{bmatrix} 0 \\ \Delta\boldsymbol{\omega}_b \end{bmatrix} - \frac{1}{2}\begin{bmatrix} 0 \\ \hat{\boldsymbol{\omega}}_b \end{bmatrix} \otimes \Delta\boldsymbol{Q}_b \quad , \qquad (25)$$

In the equation, $\Delta\boldsymbol{\omega}_b$ represents the difference between the true angular velocity and the estimated angular velocity of the SC:

$$\Delta\boldsymbol{\omega}_b = \boldsymbol{\omega}_b - \hat{\boldsymbol{\omega}}_b \quad , \qquad (26)$$

Considering that the attitude and angular velocity deviations are small, by neglecting higher-order terms, the equation (25) can be linearized as:

$$\Delta\dot{q}_0 = 0 \quad , \qquad (27)$$

$$\Delta\dot{\mathbf{q}}_v = -\hat{\omega}_b^{\times}\Delta\boldsymbol{q}_v + \frac{1}{2}\Delta\boldsymbol{\omega}_b \quad , \qquad (28)$$

From the equation, it can be seen that the dynamics of the error quaternion naturally reduce to a linear equation represented by three independent variables, avoiding singularity issues in the error covariance matrix during filtering.

Therefore, the linearized equation for the system state estimation error is:

$$\Delta\dot{\mathbf{X}} = \boldsymbol{F}\Delta\boldsymbol{X} + \boldsymbol{G}\boldsymbol{W} \quad , \qquad (29)$$

In the equation,

$$\Delta\boldsymbol{X} = \begin{bmatrix} \Delta\boldsymbol{X}_1 \\ \Delta\boldsymbol{X}_2 \end{bmatrix}, \boldsymbol{F} = \begin{bmatrix} \boldsymbol{F}_{k1} & \boldsymbol{F}_{k2} \\ \Omega & \boldsymbol{0}_{16} \end{bmatrix} \quad ,$$

$$\boldsymbol{G} = \begin{bmatrix} \boldsymbol{E}_{16} & \\ & \boldsymbol{M}^{-1} \end{bmatrix}, \boldsymbol{W} = \begin{bmatrix} \boldsymbol{\eta}_q \\ \boldsymbol{\eta}_d \end{bmatrix} \quad ,$$

$$\boldsymbol{F}_{k1} = \begin{bmatrix} \boldsymbol{0}_{12} & & \\ & -\hat{\omega}_b^{\times} & \\ & & 0 \end{bmatrix}, \boldsymbol{F}_{k2} = \begin{bmatrix} \boldsymbol{E}_{12} & & \\ & \frac{1}{2}\boldsymbol{E}_3 & \\ & & 1 \end{bmatrix} \quad ,$$

3.4.2 Measurement Equations

For the observation equations of the inertial sensors and MOSA2 rotation angles, under the small displacement assumption, the difference between the measured values and the estimated values of each state variable is:

$$\Delta\boldsymbol{x}_{tm}^{m} = \boldsymbol{x}_{tm}^{m} - \hat{\mathbf{x}}_{tm} \quad , \qquad (30)$$

$$\Delta\alpha_{bT2}^{m} = \alpha_{bT2}^{m} - \hat{\alpha}_{bT2} \quad , \qquad (31)$$

For the observation equations of the star tracker, let the difference between the measured and estimated attitude quaternions be:

$$\Delta\boldsymbol{Q}_b^{m} = \hat{\mathbf{Q}}_b^{-1} \otimes \boldsymbol{Q}_b \quad , \qquad (32)$$

When the measured values are close to the estimated values, we have:

$$\Delta\boldsymbol{Q}_b^{m} \approx \begin{bmatrix} 1 \\ \Delta\boldsymbol{q}_v^{m} \end{bmatrix} \quad , \qquad (33)$$

By substituting equations (4) and (24) into the equation (32), we obtain:

$$\Delta\boldsymbol{Q}_b^{m} = \Delta\boldsymbol{Q}_b \otimes \boldsymbol{Q}_n \quad , \qquad (34)$$

By substituting equations (5) and (33) into the above equation and neglecting higher-order terms, the linearized measurement deviation equation can be obtained:

$$\Delta\boldsymbol{q}_v^{m} = \Delta\boldsymbol{q}_v + \boldsymbol{\eta}_{str} \quad , \qquad (35)$$

Therefore, the linearized equation for the system measurement estimation error is:

$$\Delta\boldsymbol{Y} = \boldsymbol{H}\Delta\boldsymbol{X} + \boldsymbol{V} \quad , \qquad (36)$$

In the equation,

$$\Delta\boldsymbol{Y} = \begin{bmatrix} \Delta\boldsymbol{x}_{tm}^{m} \\ \Delta\boldsymbol{q}_v^{m} \\ \Delta\alpha_{bT2}^{m} \end{bmatrix}, \boldsymbol{H} = \begin{bmatrix} \boldsymbol{E}_{16} & \boldsymbol{0}_{16} \end{bmatrix}, \boldsymbol{V} = \begin{bmatrix} \boldsymbol{\eta}_{grs} \\ \boldsymbol{\eta}_{str} \\ \eta_{mosa} \end{bmatrix} \quad ,$$

3.4.3 Filtering Algorithm

Based on the derived state equations (19), state estimation error equations (29), and measurement deviation equations (36), after discretization, Kalman filtering method is employed for attitude estimation. The algorithm proceeds as follows:

1. State Prediction:

Before sensor measurements are available, the predicted values of the state variables are calculated according to the equations:

$$\boldsymbol{X}(k+1|k)=(\boldsymbol{E}+\boldsymbol{A}_k\Delta t)\boldsymbol{X}(k|k)+\Delta t\boldsymbol{B}_k\boldsymbol{U}(k)\quad, \tag{37}$$

the predicted value of the attitude quaternion in $\boldsymbol{X}(k+1|k)$ is denoted as $\boldsymbol{Q}_b(k+1|k)$:

The predicted calculation of the error covariance matrix is:

$$\boldsymbol{P}(k+1|k)=\boldsymbol{F}_{step}\boldsymbol{P}(k|k)\boldsymbol{F}_{step}^{\mathrm{T}}+\boldsymbol{G}_{step}\boldsymbol{Q}_k\boldsymbol{G}_{step}^{\mathrm{T}}\quad, \tag{38}$$

In the equation:

$$\boldsymbol{F}_{step}=\boldsymbol{E}+\Delta t\boldsymbol{F}\quad,$$

$$\begin{aligned}\boldsymbol{G}_{step}&=\int_0^{\Delta t}\boldsymbol{F}_{step}(\boldsymbol{X}_{k/k},\tau)\boldsymbol{G}d\tau\\&=\int_0^{\Delta t}(\boldsymbol{E}+\tau\boldsymbol{F})\boldsymbol{G}d\tau\\&=\boldsymbol{G}\Delta t+\tfrac{1}{2}\boldsymbol{F}\boldsymbol{G}\Delta t^2\end{aligned}\quad,$$

2. State Update

Using the measurements provided by the sensors, the Kalman gain and the updated error covariance are computed as follows:

$$\boldsymbol{K}_{k+1}=\boldsymbol{P}(k+1|k)\boldsymbol{H}^{\mathrm{T}}\times\left[\boldsymbol{H}\boldsymbol{P}(k+1|k)\boldsymbol{H}^{T}+\boldsymbol{R}\right]^{-1}\quad, \tag{39}$$

$$\begin{aligned}&\boldsymbol{P}(k+1|k+1)=\boldsymbol{K}_{k+1}\boldsymbol{R}\boldsymbol{K}_{k+1}^{\mathrm{T}}+\\&(\boldsymbol{E}-\boldsymbol{K}_{k+1}\boldsymbol{H})*\boldsymbol{P}(k+1|k)(\boldsymbol{E}-\boldsymbol{K}_{k+1}\boldsymbol{H})^{T}\end{aligned}\quad, \tag{40}$$

$\boldsymbol{R}$ is the measurement noise matrix.

The state estimation error is:

$$\Delta\boldsymbol{X}(k+1)=\boldsymbol{K}_{k+1}(z_{k+1}-\hat{\boldsymbol{z}}_{k+1/k})\quad, \tag{41}$$

The estimated error of the quaternion vector in $\hat{\boldsymbol{z}}_{k+1/k}=\boldsymbol{H}\boldsymbol{X}(k+1|k)$ and $\Delta\boldsymbol{X}(k+1)$ is denoted as $\Delta\boldsymbol{q}_v(k+1)$.

3. State Correction

The predicted state values are corrected using the estimated errors. Except for the attitude quaternion, the other state variables are updated as follows:

$$\boldsymbol{X}(k+1|k+1)=\boldsymbol{X}(k+1|k)+\Delta\boldsymbol{X}(k+1)\quad, \tag{42}$$

The SC attitude quaternion state is updated as:

$$\boldsymbol{Q}_b(k+1|k+1)=\boldsymbol{Q}_b(k+1|k)\otimes\begin{bmatrix}1\\ \Delta\boldsymbol{q}_v(k+1)\end{bmatrix}\quad, \tag{43}$$

In summary, the spacecraft attitude and related system states can be solved in real time through recursive estimation. The estimated attitude is used in place of the star tracker measurements to calculate the pointing error, which is fed back to the controller to form a closed-loop system. Based on previous research, the controller is designed using the mixed-sensitivity approach of H_∞ robust control theory. The Structure for control loops is shown in Fig. 6, For detailed procedures, refer to the references [16].

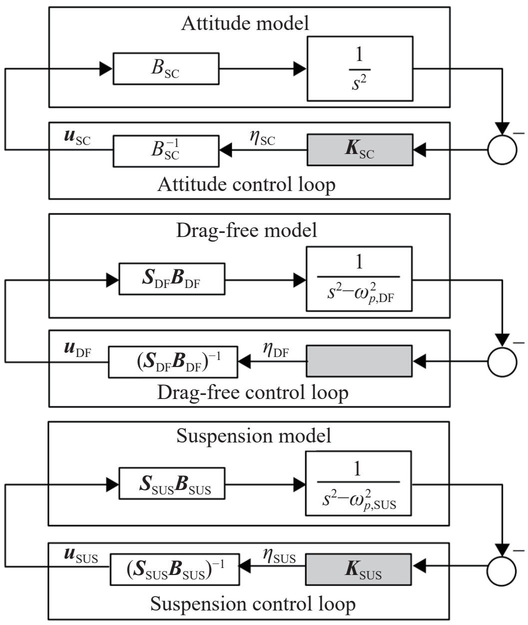

Fig. 6 schematic diagram of the control scheme [16]

4 Simulation Analysis

4.1 Simulation System

The feasibility and effectiveness of the designed pointing control scheme are verified based on a closed-loop simulation of a three-spacecraft laser link system. The simulation system parameters are shown in table1.

Tab. 1 Parameters of Simulation System

Item		Value
Duration		4000s
Step-size		0.1s
Environmental Noise		solar radiation pressure noise
Gravitational Perturbations		the sun and the eight planets
Sensor Configuration	Star Tracker:	FoV: 17.5°×13.5° Accuracy: 15μrad
	Inertial Sensor	Noise: Fig.3
Actuator Configuration	Thruster	Range: 1~100μN Resolution: 0.1μN Noise: 0.1μN/Hz$^{1/2}$
	Inertial Sensor	Noise: 1×10^{-14} N/Hz$^{1/2}$
Spacecraft Parameters	Spacecraft Mass	700kg
	Spacecraft Moment of Inertia	$\begin{bmatrix} 450 & & \\ & 450 & \\ & & 450 \end{bmatrix} kg\cdot m^2$
	TM mass	1.96kg
	TM Moment of Inertia	$\begin{bmatrix} 6.9 & & \\ & 6.9 & \\ & & 6.9 \end{bmatrix} 10^{-4} kg\cdot m^2$

The system structure is shown in the Fig 7. It consists of three independent single-spacecraft systems running in parallel, with inter-spacecraft laser links simulated through a delay module representing a 3-million-kilometer transmission. Each single-spacecraft system includes dynamics model, sensors, actuators, a DFACS controller, and a navigation and guidance module. The lead-angle compensation, state estimation, and error calculation studied in this paper are all implemented within the navigation and guidance module.

Taking inter-spacecraft laser link establishment of spacecrafts A and B as an example, the proposed high-precision pointing scheme is verified through simulation, The framework of the closed-loop is shown in Fig.8.

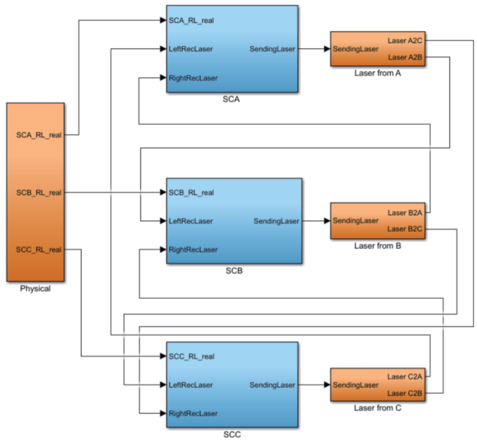

(a) Formation simulation system

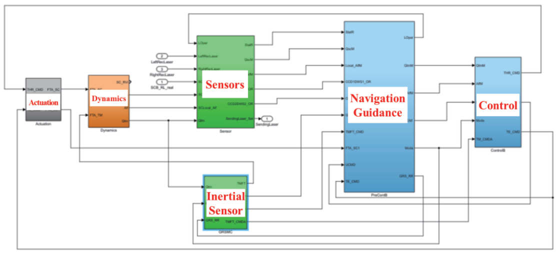

(b) Spacecraft simulation system

Fig. 7 Simulation system of formation and spacecraft

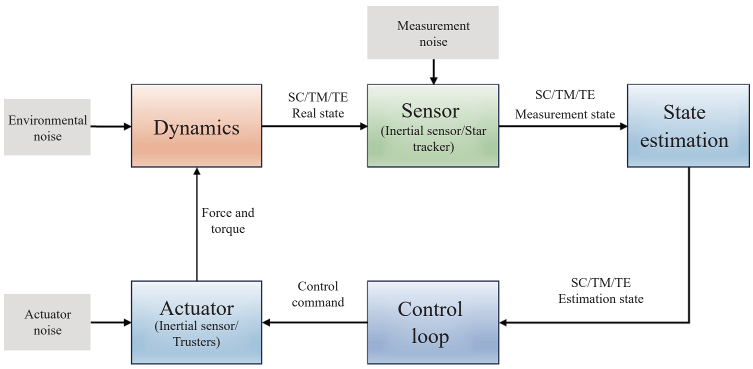

Fig. 8 The framework of the closed-loop

4.2 Simulation Results

Fig. 9 shows the variations of the measured, true, and estimated Euler angles of the SC during the simulation process, along with corresponding enlarged views. Fig. 10 presents the variations of the measurement errors and estimation errors, also with corresponding enlarged views. It can be seen that the designed attitude estimator significantly suppresses the impact of star tracker measurement noise, achieving high-precision real-time attitude estimation. Moreover, the estimated attitude values track the spacecraft's true attitude changes more smoothly compared to the measured values.

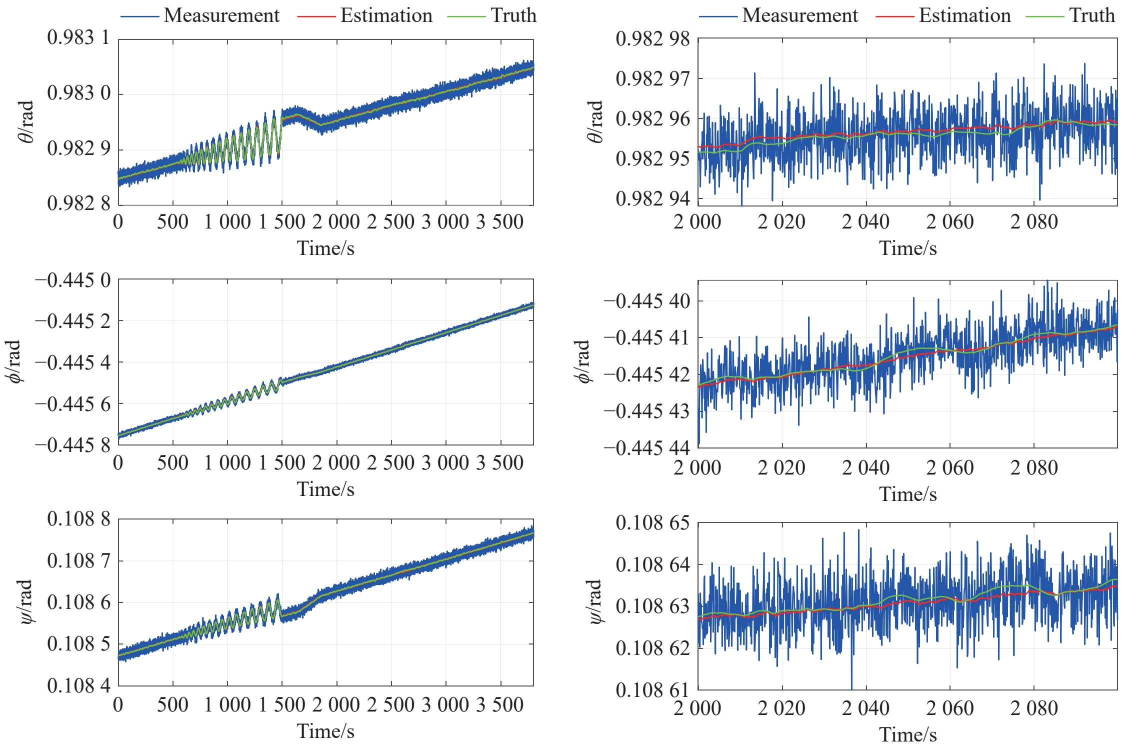

Fig. 9 Variations of the Euler angles of the SC

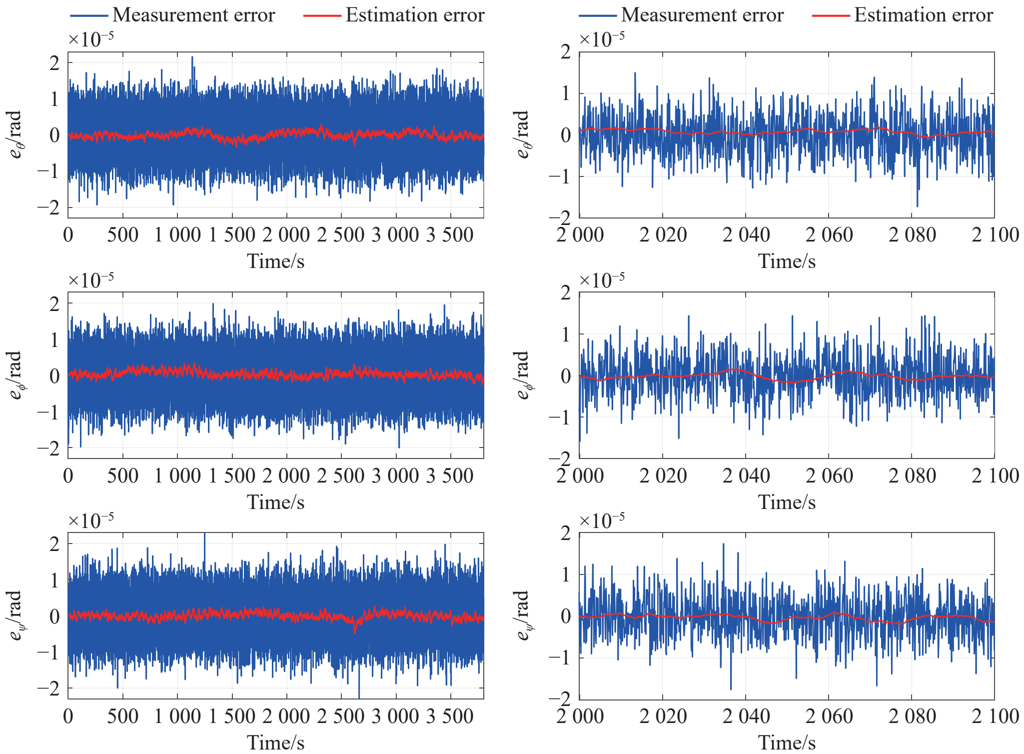

Fig. 10 Attitude Measurement error and Estimation error

To evaluate the performance of the designed attitude state estimator, a performance metric, error compression ratio, is defined as:

$$\mathrm{ERR} = \frac{\bar{e}_m - \bar{e}_e}{\bar{e}_m} \times 100\% \quad , \qquad (44)$$

The estimation performance statistics calculated are shown in the table2. It can be seen that the attitude estimation errors are all reduced by an order of magnitude compared to the measurement errors, with corresponding error compression ratios exceeding 80%. The estimation results provide the pointing controller with higher-precision attitude navigation information.

Tab. 2 Performance of the estimator for SC attitude

State Variables	x/rad	y/rad	z/rad
$\bar{e}_m$	4.99×10^{-6}	5.02×10^{-6}	5.01×10^{-6}
$\bar{e}_e$	8.96×10^{-7}	9.57×10^{-7}	9.17×10^{-7}
ERR	82.04%	80.94%	81.70%

Closed-loop simulations were conducted using the attitude measurements and the estimated values as control inputs, combined with the designed robust disturbance-rejection controller. The resulting attitude control time-domain curves and error power spectral density plots are shown in Fig. 11. It can be seen that when the estimated attitude is used as the control input, the resulting control errors are significantly smaller than those obtained when using the measured values directly. This verifies that the proposed MEKF-based pointing control scheme can achieve high-precision pointing for GW detection spacecrafts.

In the reference [12], a pseudo-linear measurement is constructed by an approximate transformation for quaternion measurements under small angle change of the spacecraft to deal with the same problem of attitude estimation. Comparing the estimation accuracy of the two methods, it is obviously from the time-domain and frequency-domain diagram that the proposed method in this paper achieves higher error compression ratios, which illustrates the superiority of the proposed algorithm.

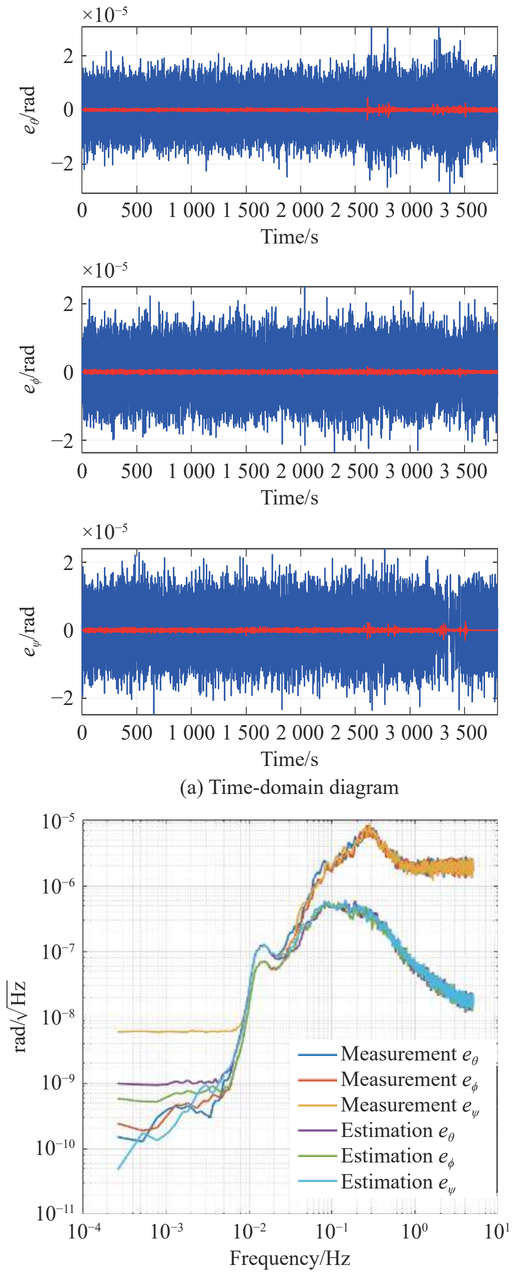

(a) Time-domain diagram

(b) Power spectral density diagram

Fig. 11 Control error of the spacecraft attitude

5 Conclusion

This paper investigates the problem of high-precision beam pointing control for inter-spacecraft laser link establishment in space-borne GW detection spacecraft, based on multi-source information fusion. An analytical expression for the laser PAA was derived, a Kalman-filter-based attitude estimator with a globally linearized quaternion measurement model was developed to enable real-time, high-precision attitude estimation. Together with a robust disturbance rejection controller, the proposed approach achieved accurate beam pointing and link acquisition. Considering the structural and payload characteristics of the GW detection spacecraft, a complete system state equation including MOSA motion was established. By introducing the error quaternion, the nonlinear attitude measurement equations with dependent variables were transformed into linear equations with independent variables, and the fusion of inertial sensor measurements was employed to improve the attitude estimation accuracy. In addition, the time-varying analytical expression of the PAA was derived to address the effects of ultra-long inter-spacecraft laser transmission delay and high relative velocity, and the variation trend of the PAA within one orbital period was analyzed through simulation. This provides a theoretical basis for PAA servo compensation during inter-spacecraft laser link acquisition and maintenance.

Finally, a closed-loop simulation of the laser link acquisition process among the three spacecraft validated the proposed high-precision pointing estimation algorithm, confirming its advantages in both stability and estimation accuracy. In combination with the robust disturbance-rejection controller, accurate beam pointing was realized, thus offering critical technical support for the execution of space-borne GW detection mission.

References:

[1] 陈沛权, 邓汝杰, 张艺斌, 等. 太极计划星间激光通信测距的伪随机码选取[J]. 中国光学 (中英文), 2025, 18(3): 547-556.
CHEN P Q, DENG R J, ZHANG Y B, *et al*.. Pseudo-random code selection for inter-satellite laser ranging and data communication in the Taiji program[J]. *Chinese Optics*, 2025, 18(3): 547-556. (in Chinese).

[2] 胡越欣, 张立华, 高永, 等. 空间引力波探测航天器关键技术分析[J]. 航天器工程, 2022, 31(4): 1-7.
HU Y X, ZHANG L H, GAO Y, *et al*.. Analysis of key technologies of spacecraft for gravitational waves detection in space[J]. *Spacecraft Engineering*, 2022, 31(4): 1-7. (in Chinese).

[3] The Taiji Scientific Collaboration. China's first step towards probing the expanding universe and the nature of gravity using a space borne gravitational wave antenna[J]. *Communications Physics*, 2021, 4(1): 34.

[4] 罗子人, 张敏, 靳刚, 等. 中国空间引力波探测"太极计划"及"太极 1 号"在轨测试[J]. 深空探测学报, 2020, 7(1): 3-10.
LUO Z R, ZHANG M, JIN G, *et al*.. Introduction of Chinese space-borne gravitational wave detection program "Taiji" and "Taiji-1" satellite mission[J]. *Journal of Deep Space Exploration*, 2020, 7(1): 3-10. (in Chinese).

[5] LUO J, CHEN L SH, DUAN H Z, *et al*.. TianQin: a space-borne gravitational wave detector[J]. *Classical and Quantum Gravity*, 2016, 33(3): 035010.

[6] WANG S, LIU H S, ZHOU Z B, *et al*. . In-orbit performance of the inertial sensor on TianQin-1 satellite[J]. *Measurement Science and Technology*, 2022, 33(3): 035012. **(查阅网上资料, 未找到本条文献信息, 请确认)**.

[7] 吴树范, 王楠, 龚德仁. 引力波探测科学任务关键技术[J]. 深空探测学报, 2020, 7(2): 118-127.
WU SH F, WANG N, GONG D R. Key technologies for space science gravitational wave detection[J]. *Journal of Deep Space Exploration*, 2020, 7(2): 118-127. (in Chinese).

[8] JIAO B H, LIU Q F, DANG ZH H, *et al*.. A review on DFACS (I): System design and dynamics modeling[J]. *Chinese Journal of Aeronautics*, 2024, 37(5): 92-119.

[9] 方子若, 朱振才, 蔡志鸣, 等. 空间引力波探测航天器光学测距噪声链路指标优化[J]. 中国光学 (中英文), 2025, 18(3): 568-582.
FANG Z R, ZHU ZH C, CAI ZH M, *et al*.. Optimization of optical metrology noise link metrics for space-based gravitational wave detection spacecraft[J]. *Chinese Optics*, 2025, 18(3): 568-582.

[10] HEISENBERG L, INCHAUSPÉ H, NAM D Q, *et al*.. LISA dynamics and control: closed-loop simulation and numerical demonstration of time delay interferometry[J]. *Physical Review D*, 2023, 108(12): 122007.

[11] 叶磊巧, 杜明辉, 徐鹏, 等. 空间引力波探测"太极计划"星间姿态-光程耦合噪声迭代拟合与高精度抑制方法[J]. 中

国光学(中英文), 2025, 18(3): 583-595.

YE L Q, DU M H, XU P, *et al*.. Iterative estimation and precision suppression of inter-spacecraft tilt-to-length coupling noise for the Taiji space gravitational wave detection mission[J]. *Chinese Optics*, 2025, 18(3): 583-595. (in Chinese).

[12] 张东林, 曹一凡, 段战胜, 等. 空间引力波探测航天器高精度状态估计器设计[J]. 深空探测学报(中英文), 2023, 10(5): 557-564.

ZHANG D L, CAO Y F, DUAN ZH SH, *et al*.. High precision state estimation method design for space-based gravitational wave detection spacecraft[J]. *Journal of Deep Space Exploration*, 2023, 10(5): 557-564. (in Chinese).

[13] JIAO Y Y, ZHOU H Y, WANG J Q, *et al*.. Linearization error's measure and its influence on the accuracy of MEKF based attitude determination method[J]. *Aerospace Science and Technology*, 2012, 16(1): 61-69.

[14] HOUBA N, DELCHAMBRE S, ZIEGLER T, *et al.* . LISA point-ahead angle control for optimal tilt-to-length noise estimation[J]. arXiv preprint arXiv: 2208.11033, 2022. **(查阅网上资料, 不确定本文献类型是否正确, 请确认)**.

[15] WANG D ZH, ZHANG X F, DUAN H Z. On point-ahead angle control strategies for TianQin[J]. *Classical and Quantum Gravity*, 2024, 41(11): 117003.

[16] 范一迪, 王鹏程, 卢苇, 等. 双检验质量无拖曳卫星鲁棒控制[J]. 深空探测学报(中英文), 2023, 10(3): 310-321.

FAN Y D, WANG P CH, LU W, *et al*.. Robust controller design for drag-free satellites with two test masses[J]. *Journal of Deep Space Exploration*, 2023, 10(3): 310-321. (in Chinese).

Author Biographies:

GUO Ming (1991—), male, born in Laiwu, Shandong Province. Ph.D. candidate at the Innovation Academy for Microsatellites, Chinese Academy of Sciences, his research mainly focuses on spacecraft system design. Email: guom@microsate.com

FAN Yi-di (1993–), female, born in Lianyungang, Jiangsu Province. She received her Ph.D. from the Harbin Institute of Technology and is now an assistant research fellow. Her research focuses on spacecraft dynamics and control. Email: fanyd@microsate.com